J. Iron Steel Res. Int. (2024) 31:1376–1388
https://doi.org/10.1007/s42243-023-01037-w

ORIGINAL PAPER

Interaction mechanism between $BaZrO_3/Y_2O_3$ refractory and Ti_2Ni alloy melts

Xiao Hou[1] · Guang-yao Chen[1,2,3] · Jian Liu[1] · Ming-rui Lv[1] · Fei-hai Yu[1] · Qi-sheng Feng[1] · Rong-bin Li[4] · Xiong-gang Lu[2,4] · Chong-he Li[1,2,3]

Received: 20 February 2023 / Revised: 7 May 2023 / Accepted: 17 May 2023 / Published online: 29 July 2023

Abstract

The titanium alloys with highly chemical activity require stable crucible refractories that can withstand the erosion of alloy melts. The phase composition and microstructure are crucial factors that affect the stability of the refractory crucible. The effect of Y_2O_3 on the composition and microstructure of $BaZrO_3$ crucible was systematically investigated, and the improved mechanism of the stability of $BaZrO_3/Y_2O_3$ crucible was clarified in comparison with the $BaZrO_3$ crucible. The results showed that the erosion layer thickness of the $BaZrO_3/Y_2O_3$ crucible was only 63 μm, which was far less than that in the $BaZrO_3$ crucible (485 μm), and the erosion layer in the $BaZrO_3/Y_2O_3$ crucible also exhibited a higher density than that in the $BaZrO_3$ crucible. During the sintering, Y_2O_3 could improve the densification of the $BaZrO_3$ crucible due to the solid solution effect between Y_2O_3 and ZrO_2, which also caused the evaporation of BaO, resulting in the generation of a Y_2O_3 (ZrO_2) film on the surface of the crucible. Furthermore, the Y_2O_3 (ZrO_2) had higher thermodynamic stability than Y_2O_3, confirming that the $BaZrO_3/Y_2O_3$ crucible with high density exhibited a superior erosion resistance to titanium alloys. This dual-phase structure provides a strategy to design a long-life and stable refractory for melting titanium alloys.

Keywords Barium zirconate · Yttrium oxide · Dual-phase refractory · Titanium alloy · Interaction

1 Introduction

Titanium alloys attract the attention due to their high specific strength, corrosion resistance [1, 2] and biocompatibility [3]. However, their extensive use for civilian applications is still hindered by the high costs associated with complicated metallurgical processing [4]. Fortunately, the vacuum induction melting method can help to reduce the production costs of titanium alloys [5]. Additionally, the key challenge is to select a suitable refractory to contain the molten titanium alloys [6].

Common oxides, such as Al_2O_3 [7, 8], ZrO_2 [9], CaO [10] and Y_2O_3 [11, 12], have demonstrated higher corrosion resistance in contact with titanium alloys than carbide, nitride and boride ceramics [13]. However, none of these materials proves to be totally inert against titanium alloy melts. Recently, a perovskite structure material, $CaZrO_3$ [14, 15] or $BaZrO_3$, shows good potential as an alternative refractory [16].

Functional thin $CaZrO_3$ coatings obtained by centrifuging and spraying according to the replica technique improve the properties of titanium alloy casting molds [17]. Schafföner et al. [18] demonstrated that $CaZrO_3$ exhibits good corrosion resistance in contact with titanium alloy melts. In addition, self-prepared shell molds based on $CaZrO_3$ ceramic are better than commercial shell systems [19].

✉ Guang-yao Chen
cgybless1@shu.edu.cn

✉ Chong-he Li
chli@staff.shu.edu.cn

[1] State Key Laboratory of Advanced Special Steel and Shanghai Key Laboratory of Advanced Ferromeallurgy and School of Materials Science and Engineering, Shanghai University, Shanghai 200072, China

[2] Shanghai Special Casting Engineering Technology Research Center, Shanghai 201605, China

[3] Zhejiang Institute of Advanced Materials, Shanghai University, Jiashan 314100, Zhejiang, China

[4] School of Materials Science and Engineering, Shanghai DianJi University, Shanghai 201306, China

A study by Gao et al. [20] revealed that the shape-memory TiNi alloy prepared using the $BaZrO_3$ crucible could achieve a higher shape-memory rate and fatigue life than that prepared using the graphite crucible. In addition, the TiAl alloy prepared using the $BaZrO_3$ crucible exhibited a higher purity than that using the MgO and Al_2O_3 crucibles on the laboratory scale [21]. Furthermore, a pilot-scale preparation of TiAl alloy was also achieved in the $BaZrO_3$ crucible [22].

In fact, the difficulties of the metallurgy of titanium alloys with a refractory crucible lie in the contamination of alloys and the erosion of the refractory crucible. These phenomena will get worse with the increase in titanium content in the alloys due to the increased chemical activity. The researchers found that the $BaZrO_3$ refractory exhibited insufficient stability during melting the alloys with high titanium content, confirming serious oxygen contamination in the alloy and damage to the crucible [23]. It limits the further application of the $BaZrO_3$ refractory. Thus, to improve the stability of $BaZrO_3$ refractories, it is necessary to broaden its extent of melting titanium alloys.

Several composite molds, including Y_2O_3–Al_2O_3–MgO–CaO [24], BN–ZrO_2 [25] and ZrO_2–M_xO_y (M = La, Ce, and Nb) [26], have been proposed. In our previous study, we proposed an effective strategy for designing a dual-phase material using Y_2O_3 and $BaZrO_3$ [27]. This material was able to maintain the stability of both $BaZrO_3$ and Y_2O_3, and the dissolution of Y_2O_3 in $BaZrO_3$ leads to the formation of a solid-solution phase $BaZr_{1-x}Y_xO_{3-\delta}$, which improved the stability of the refractory. Kuang et al. [28] demonstrated that the penetration of alloy melts into the refractory is related to the wettability, and a theoretical calculation by Zheng et al. [29] indicated that the non-wettability performance of $BaZrO_3$ refractory was better than that of Y_2O_3 refractory when in contact with TiAl alloy melts.

Although the previous study also revealed that the $BaZrO_3/Y_2O_3$ refractory exhibited good performance in the process of melting the TiAl alloys [27]. However, the effect of Y_2O_3 on the phase composition and microstructure of $BaZrO_3$ crucibles has not been thoroughly studied, and the activity of Ti in the TiAl alloy melt is insufficient to obtain a significant difference in the interaction between the refractory and TiAl alloys. In this study, the phase composition and microstructure of the surface and the cross-section of $BaZrO_3/Y_2O_3$ crucible were carefully investigated, and the interaction mechanism between the $BaZrO_3/Y_2O_3$ crucible and a high titanium content Ti_2Ni alloy was further clarified in comparison with the $BaZrO_3$ crucible. The basic research focused on the dual-phase refractory may help meet future demands for melting titanium alloys.

2 Experimental

2.1 Preparation of crucibles

In this study, two different types of crucibles made of fused $BaZrO_3$ powder (size of 13 μm, Shandong Haoyao New Material Co., Ltd., Shandong, China) and commercial Y_2O_3 powder (purity of 99.9%, size of 5 μm, Sinopharm Chemical Regent Co., Ltd., Shanghai, China) were designed and produced. To prepare the $BaZrO_3/Y_2O_3$ dual-phase crucible, according to previous research results [27], the ingredients were weighed carefully according to the molar ratio of $BaZrO_3$ toY_2O_3 of 2:1. In order to mix the ingredients well, the raw materials were first mixed in alcohol, ball-milled on a ball mill for 8 h, and finally dried at 120 °C for 12 h. As shown in Fig. 1, the dried raw material was isostatically cold pressed for 3 min at a pressure of 150 MPa in a U-shaped crucible mold and pressed into a green body. Finally, the $BaZrO_3/Y_2O_3$ dual-phase crucibles were sintered at 1750 °C for 6 h in a Si–Mo rod sintering furnace. In addition, the preparation conditions of the $BaZrO_3$ crucible are the same as those of the $BaZrO_3/Y_2O_3$ dual-phase crucible. The $BaZrO_3$ crucible after sintering was 5.5 cm in width and 7 cm in height, and the Y_2O_3 crucible after sintering was 4.5 cm in width and 6 cm in height.

2.2 Erosion resistance test

Ti_2Ni alloys were fabricated in a water-cooled copper induction furnace using a 2:1 molar ratio of titanium sponge (99.9%) to nickel plate (99.9%). The alloys were melted in a medium frequency vacuum induction furnace with the crucibles. Before the melting, the furnace chamber was evacuated down to 10^{-3} Pa and then backfilled with pure argon up to 0.06 MPa for three times. The alloys were melted in the crucible at 1600 °C for 3 min and then poured into a graphite crucible to obtain the alloy ingots. This melting process was repeated for three times, and each crucible is used three times with each time using a different master alloy prepared from the same batch. The detailed flowchart including the preparation of refractory crucibles and the master alloys is also shown in Fig. 1. The phase composition was analyzed by X-ray diffraction (XRD) (D8 Advance, Bruker) with nickel-filtered Cu Kα radiation. The microstructure analysis was examined using a scanning electron microscope (JSM-6700F) combined with the energy-dispersive spectrometry (EDS) equipment. Inductively coupled plasma atomic emission spectrometry (ICP) and LECO TC600 O/N analyzer were utilized to examine the alloy impurity element caused by the crucible refractory. The erosion layer was measured with the Ruler

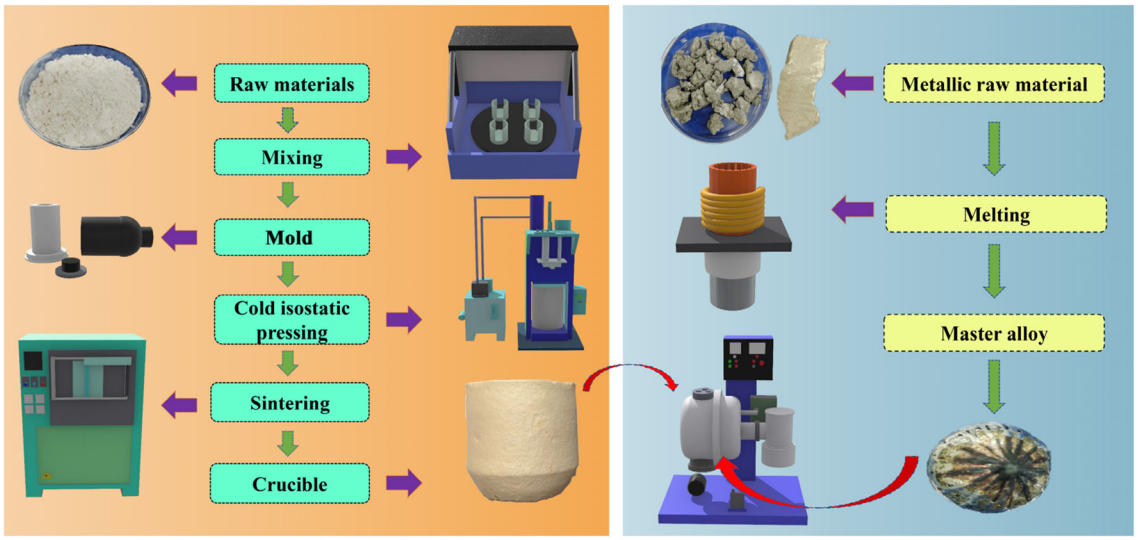

Fig. 1 Schematic diagram of preparation route of crucibles and melting experiment

software, and an average was obtained after multiple measurements.

3 Results and discussion

3.1 Phase composition and microstructure of crucibles

Figure 2 shows the scanning electron microscopy (SEM) images of the surface and inner structure of the $BaZrO_3$ and $BaZrO_3/Y_2O_3$ crucibles after sintering at 1750 °C for 6 h. Combining the EDS results in Table 1 and Fig. 2a, the surface of the $BaZrO_3$ crucible was composed of $BaZrO_3$ and ZrO_2. Our previous study revealed that ZrO_2 could be formed as a second phase during the electric arc furnace process of $BaZrO_3$ raw material due to the evaporation of BaO [27]. The backscattered electron (BSE) image shows that the amount of ZrO_2 in the surface was little. After the grinding and polishing, the interior of the $BaZrO_3$ crucible consisted of ZrO_2 (grain C) and $BaZrO_3$ (grain D), as shown in Fig. 2b, and this was consistent with the phase composition of the crucible surface. In addition, the number of pores in the surface was less than that in the interior. A study by Ahmed et al. [30] revealed that the growth of grains on the surface had more advantages due to easier elimination of pores and lower stress.

The surface of the $BaZrO_3/Y_2O_3$ crucible in Fig. 2c showed that it consisted of some grains of different shapes, marked as grain E and grain F, respectively. EDS results in Table 1 revealed that these two grains are $Ba_{1-x}Zr_{1-y}Y_yO_{3-\delta}$ and $Y_2O_3(ZrO_2)$. To confirm the distribution of Ba element in the surface of the $BaZrO_3/Y_2O_3$ crucible, an additional element mapping analysis is shown in the inset in Fig. 2c, which indicated that only 3 at.% Ba was detected, confirming the occurrence of evaporation of BaO on the surface during the sintering. As shown in Fig. 2c, the main phase of the surface of the $BaZrO_3/Y_2O_3$ crucible is $Y_2O_3(ZrO_2)$, and only a small number of $Ba_{1-x}Zr_{1-y}Y_yO_{3-\delta}$ phase distributed in it. Additionally, no pores were observed on the surface, indicating that the densification of the surface in the $BaZrO_3/Y_2O_3$ crucible was better than that in the $BaZrO_3$ crucible. Figure 2d shows the interior of the $BaZrO_3/Y_2O_3$ crucible, presenting that it also consisted of two kinds of grains, marked as grain G and grain H. EDS analysis in Table 1 exhibits that they were $Y_2O_3(ZrO_2)$ and $BaZr_{1-x}Y_xO_{3-\delta}$, resulting from the solution of ZrO_2 in Y_2O_3 and the solution of Y_2O_3 in $BaZrO_3$, respectively. Although some pores appeared in the interior of the $BaZrO_3/Y_2O_3$ crucible, the number of pores was significantly lower by comparing with the interior in the $BaZrO_3$ crucible. It confirmed that the Y_2O_3 addition was beneficial to the densification of the $BaZrO_3$ crucible.

Figure 3 illustrates the XRD patterns of the surface of the $BaZrO_3$ and $BaZrO_3/Y_2O_3$ crucibles before and after grinding and polishing. In Fig. 3a, it can be seen that the surface of the $BaZrO_3$ crucible without grinding and polishing mainly consisted of $BaZrO_3$. After grinding and polishing, the amount of second phase ZrO_2 was significantly increased, confirmed by the analysis in Fig. 2a, b. During the sintering, the low surface stress was conducive to the growth of the main phase $BaZrO_3$ grains on the surface, which also influenced the sintering of second phase ZrO_2 [31]. Figure 3b shows that the $BaZrO_3/Y_2O_3$ crucible consisted of a mixture of $BaZrO_3$ and Y_2O_3. As shown in Fig. 3c, the magnified XRD pattern of the crucible over the 2θ range of 27°–37° exhibited a significant peak shifting of $BaZrO_3$ toward lower angles. It was

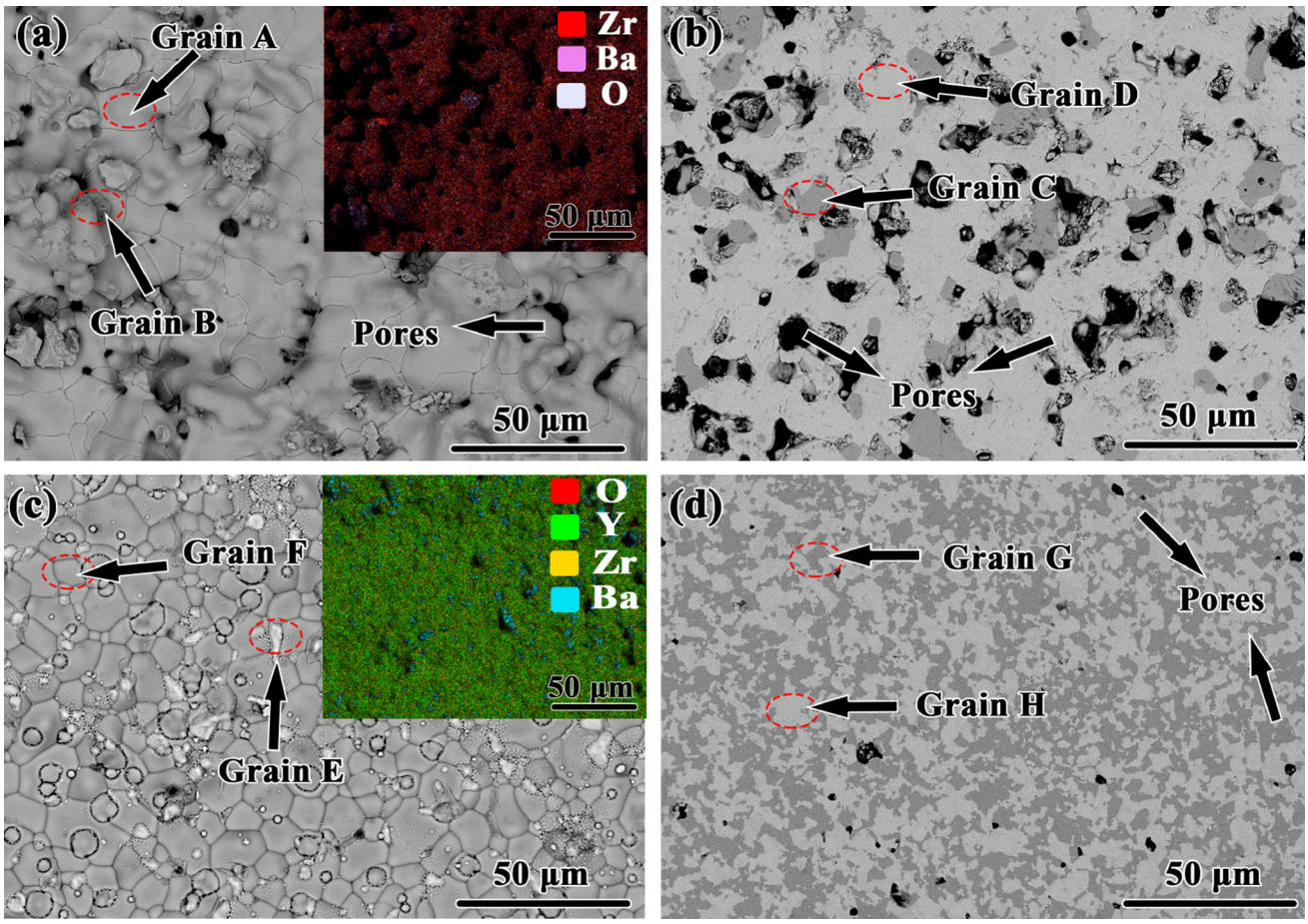

Fig. 2 SEM image of surface of $BaZrO_3$ crucible and EDS element mapping image for O, Zr, and Ba elements (**a**), interior of $BaZrO_3$ crucible after grinding and polishing (**b**), SEM image of surface of $BaZrO_3/Y_2O_3$ crucible and EDS element mapping image for O, Y, Zr, and Ba elements (**c**) and interior of $BaZrO_3/Y_2O_3$ crucible after grinding and polishing (**d**)

Table 1 EDS results of grains A–H in Fig. 2

Grain	Element content/at. %				Possible phase
	Ba	Zr	Y	O	
A	24.30	37.07	–	38.63	$BaZrO_3$
B	–	65.21	–	34.79	ZrO_2
C	–	31.93	–	68.07	ZrO_2
D	24.59	20.95	–	54.46	$BaZrO_3$
E	18.56	12.46	2.53	66.45	$Ba_{1-x}Zr_{1-y}Y_yO_{3-\delta}$
F	0.25	12.24	18.94	68.57	$Y_2O_3(ZrO_2)$
G	–	11.51	25.47	63.02	$Y_2O_3(ZrO_2)$
H	20.48	19.96	2.75	56.81	$BaZr_{1-x}Y_xO_{3-\delta}$

because the Y^{3+} ions (0.90 Å) could replace the Zr^{4+} ions (0.72 Å) in the crystal lattice of $BaZrO_3$, leading to the formation of $BaZr_{1-x}Y_xO_{3-\delta}$ solid solution [32]. According to the Bragg's law $2d\sin\theta=n\lambda$, the increase in d value would cause a decrease in θ value. Therefore, it can be concluded that the Y_2O_3 peak shifts to higher angles due to the substitution of Zr^{4+} ions by Y^{3+} ions. In addition, it can be seen from the phase diagram in Fig. 4 that ZrO_2 could dissolve in Y_2O_3 to form α-Y_2O_3. Especially for the $BaZrO_3/Y_2O_3$ crucible, the surface of the crucible before grinding and polishing had a small amount of main phase $BaZrO_3$, and it was different from the interior of the

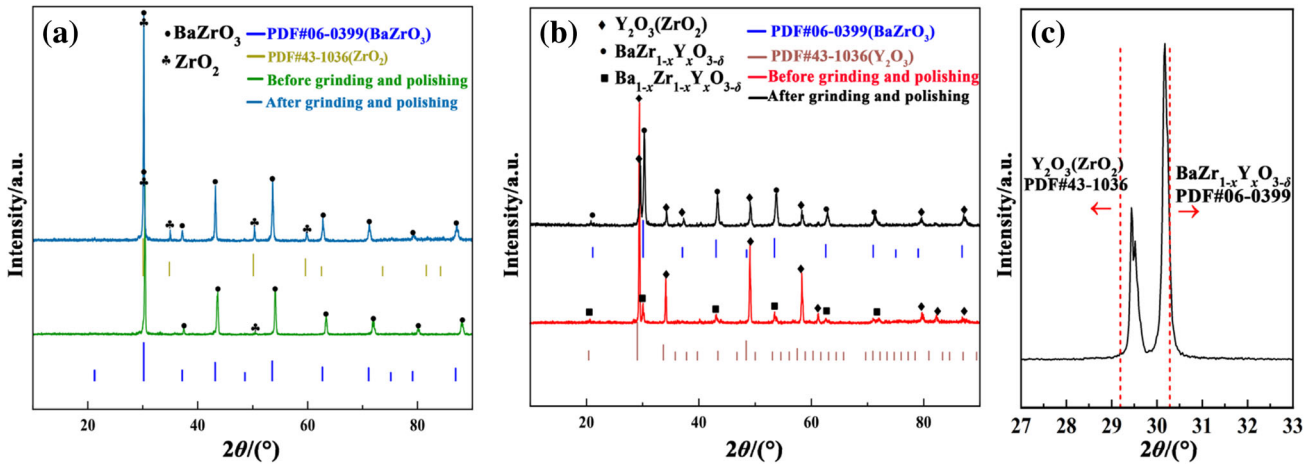

Fig. 3 XRD patterns of crucibles before and after grinding and polishing. **a** $BaZrO_3$ crucible; **b** $BaZrO_3/Y_2O_3$ crucible; **c** magnified image over 2θ range of 27°–37° in **b**

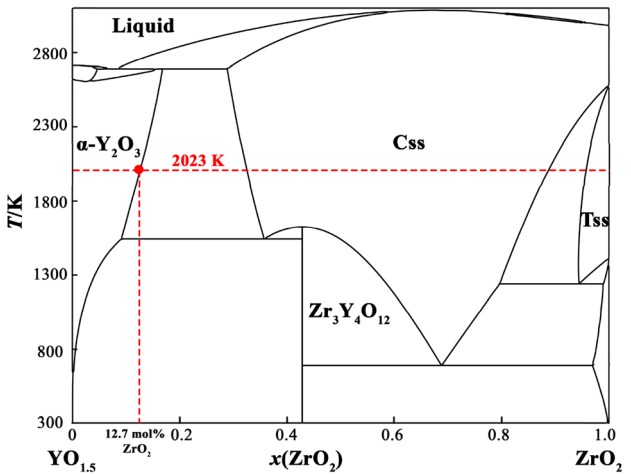

Fig. 4 $YO_{1.5}$–ZrO_2 binary diagram. *T*—Temperature; $x(ZrO_2)$—content of ZrO_2; Css—cubic structure; Tss—tetragonal structure

crucible after grinding. Thus, it can be concluded that the solid solution effect between $BaZrO_3$ and Y_2O_3 was beneficial to the evaporation of BaO [33], which was consistent with the phenomenon in Fig. 2c, d. The theoretical reactions could be used to describe the solid solution between $BaZrO_3$, ZrO_2 and Y_2O_3 below.

$$BaZrO_3 + Y_2O_3 \xrightarrow{\text{sintering,1750 °C}} BaZr_{1-x}Y_xO_{3-\delta} \quad (1)$$

$$Y_2O_3 + ZrO_2 \xrightarrow{\text{sintering,1750 °C}} Y_2O_3(ZrO_2) \quad (2)$$

$$BaZrO_3 + Y_2O_3 \xrightarrow{\text{sintering,1750 °C}} Ba_{1-x}Zr_{1-y}Y_yO_{3-\delta} + xBaO \quad (3)$$

Figure 5 depicts the cross-section of the $BaZrO_3$ and $BaZrO_3/Y_2O_3$ crucibles before the melting. From Fig. 5a, the crucible had a two-phase structure, consisting of light gray (spot 1) and black gray (spot 2) substances. EDS results in Table 2 show that they were $BaZrO_3$ (spot 1) and ZrO_2 (spot 2), respectively, confirming the analysis in the crucible surface. The element mapping in Fig. 5a shows that the two phases exhibited a good homogeneity. Additionally, some pores were significantly observed in the crucible. Figure 5b shows the cross-section of the $BaZrO_3/Y_2O_3$ crucible, and the crucible also consisted of black (spot 3) and light gray (spot 4) substances. Being different from the $BaZrO_3$ crucible in Fig. 5a, a large amount of the black gray substance was enriched along the inside wall of the $BaZrO_3/Y_2O_3$ crucible. The analysis of the element mapping in Fig. 5b exhibited that a large amount of Y and Zr elements were distributed in the black gray substance, and the deficiency of Ba element in this area confirming the occurrence of its evaporation was discussed in Figs. 2c and 3b. In comparing with the $BaZrO_3$ crucible in Fig. 5a, the Y- and Zr-rich layer had a small number of pores, indicating that it had a higher density. Additionally, this layer also had a higher densification than the crucible matrix. Thus, the Y_2O_3 addition also helped to improve the density of the $BaZrO_3$ crucible due to the effect of solid solution sintering.

3.2 Interaction between $BaZrO_3$ crucibles and Ti_2Ni alloys

Figure 6 illustrates the surface microstructure of the $BaZrO_3$ and $BaZrO_3/Y_2O_3$ crucibles before and after melting Ti_2Ni alloys. Figure 6a displays that the surface of the $BaZrO_3$ crucible before melting exhibited an even surface along with the appearance of some pores. From Fig. 6b, the surface of the $BaZrO_3$ crucible after melting was eroded by the alloy melts, leading to the appearance of the inside grains in the crucible, and a large number of pores were also observed. This was due to the destruction of the grain boundaries on the crucible surface by the

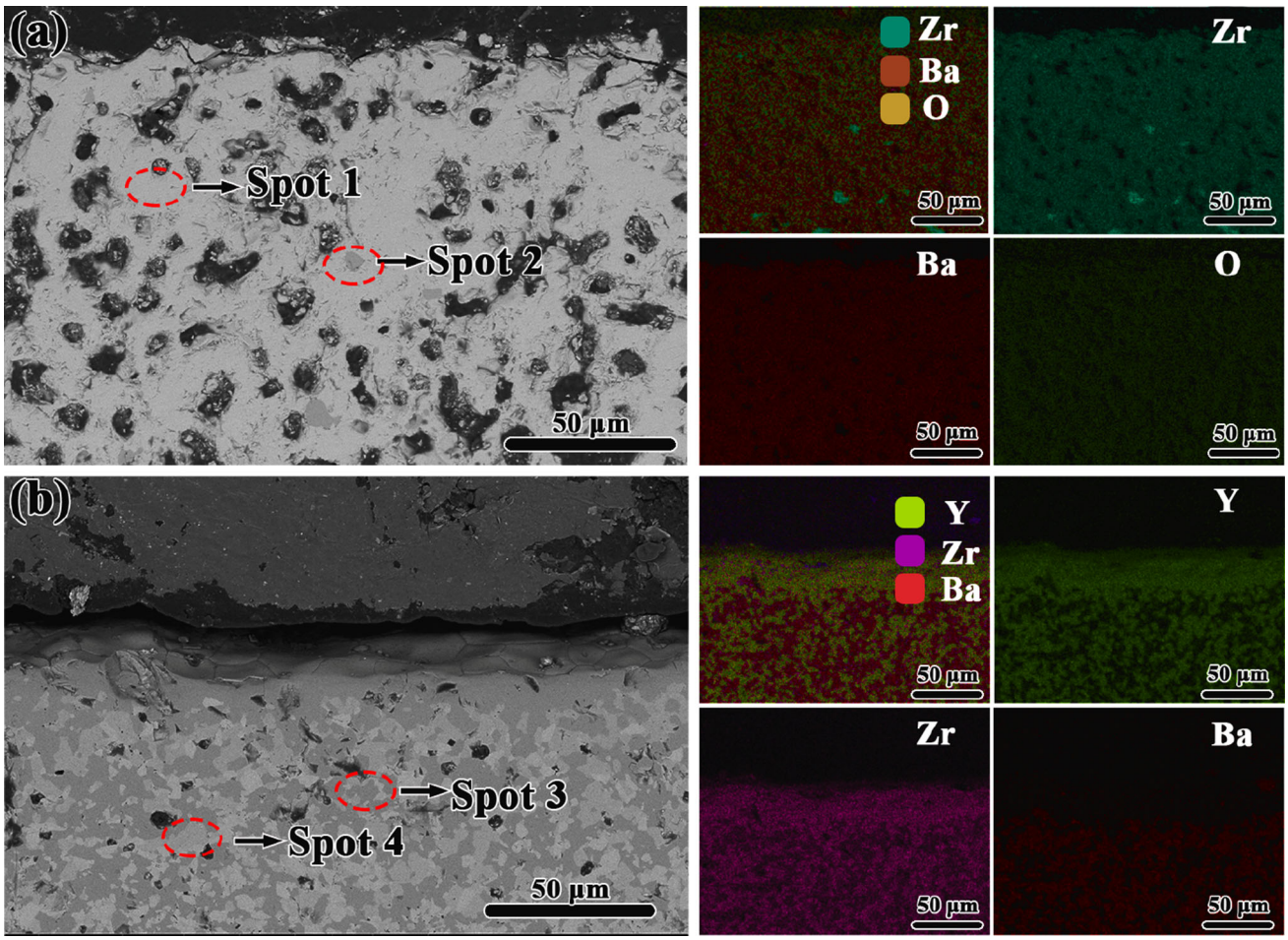

Fig. 5 SEM images and elemental mapping of cross-section of $BaZrO_3$ crucible (**a**) and $BaZrO_3/Y_2O_3$ crucible (**b**) before melting

Table 2 EDS results of spots 1–4 in Fig. 5

Spot	Element content/at.%				Possible phase
	Ba	Zr	Y	O	
1	24.03	21.03	54.93	–	$BaZrO_3$
2	–	–	33.26	66.74	ZrO_2
3	–	11.44	25.38	63.14	$Y_2O_3(ZrO_2)$
4	20.55	19.36	3.06	57.02	$BaZr_{1-x}Y_xO_{3-\delta}$

molten alloy, which then penetrated inside through the pores of the crucible, further damaging the internal structure. From Fig. 6c, the surface of the $BaZrO_3/Y_2O_3$ crucible before the melting had a complete and dense structure. From Fig. 6d, a similar erosion phenomenon was also observed in the $BaZrO_3/Y_2O_3$ crucible after the melting. However, a residual flat surface, which consisted of subsphaeroidal grains, appeared in the $BaZrO_3/Y_2O_3$ crucible. Apparently, the surface of the $BaZrO_3/Y_2O_3$ crucible was not totally damaged by the molten alloys, indicating that the Y_2O_3 addition can improve the erosion resistance of the $BaZrO_3$ crucible in the process of melting titanium alloy.

Figure 7a displays the magnified images of area I in Fig. 6d, and some subsphaeroidal grains existed on the surface of the crucible. From the surface analysis in Fig. 7b, a uniform distribution of Y and Zr elements in the subsphaeroidal grains was observed, indicating that they were $Y_2O_3(ZrO_2)$ grains. In addition, $BaZrO_3$ grains were mainly distributed inside the crucible from the distribution

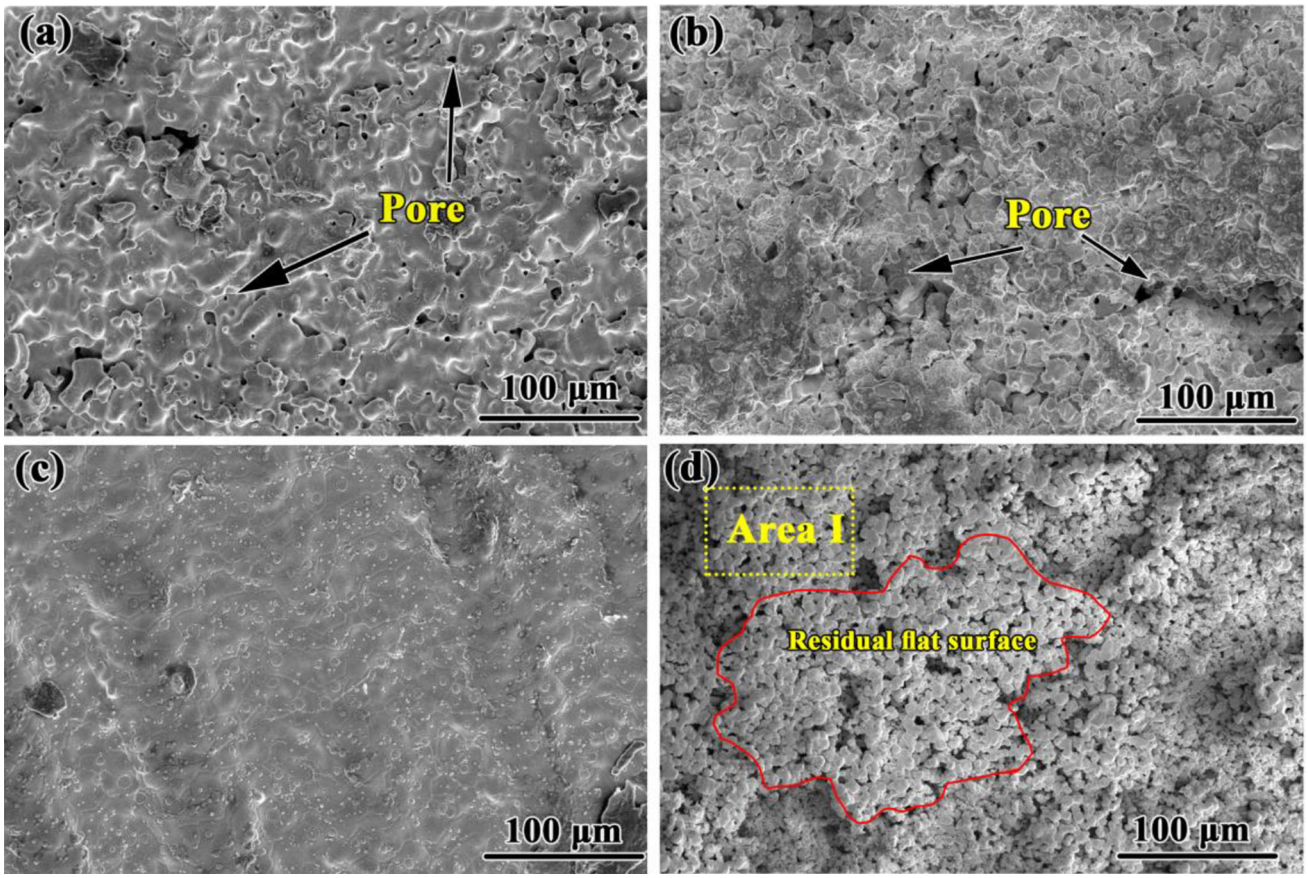

Fig. 6 SEM images of surface of crucibles before and after melting Ti_2Ni alloys. **a** $BaZrO_3$ crucible before melting; **b** $BaZrO_3$ crucible after melting; **c** $BaZrO_3/Y_2O_3$ crucible before melting; **d** $BaZrO_3/Y_2O_3$ crucible after melting

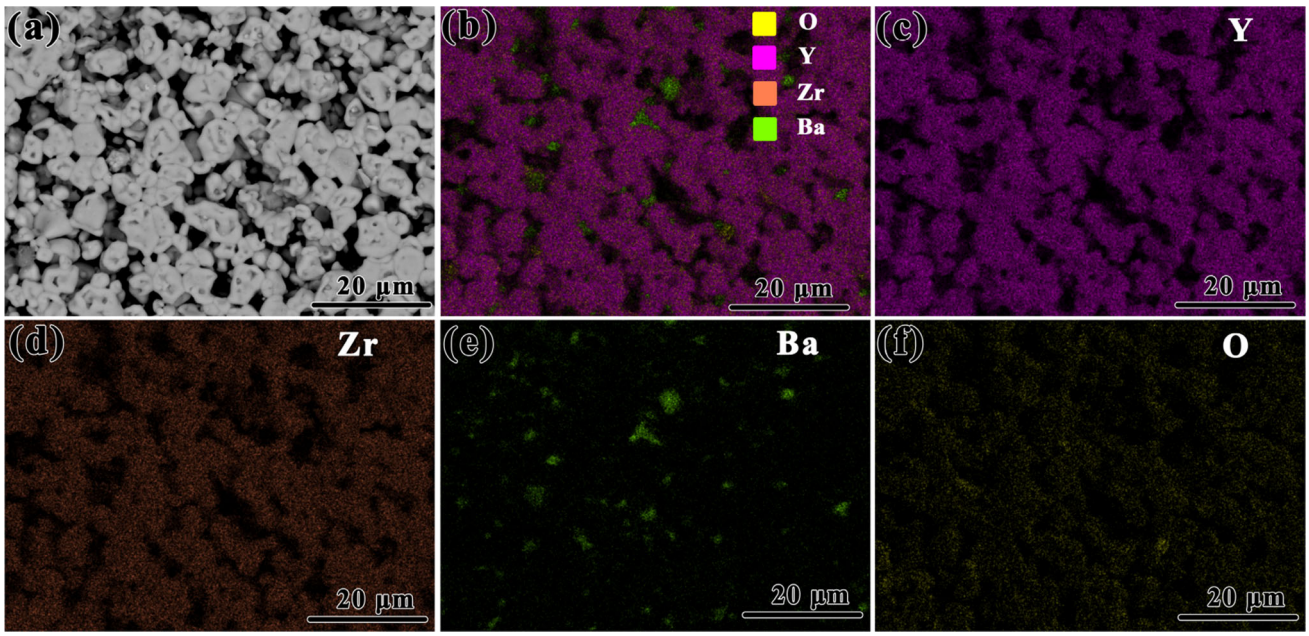

Fig. 7 Magnified image of area I in Fig. 6d (**a**), combination of all elements (**b**), and EDS element mapping images for Y, Zr, Ba, and O elements (**c**–**f**)

form of Zr and Ba elements. This suggests that the residual high-stability Y_2O_3 refractory formed a thin film in the crucible surface, which could effectively prevent the erosion by the alloy melts.

The XRD patterns of the $BaZrO_3$ and $BaZrO_3/Y_2O_3$ crucible surface before and after melting are shown in Fig. 8. From Fig. 8a, it can be seen that no other new phases were observed on the inner surface of the $BaZrO_3$ crucible after the melting. Study by Chen et al. [16] indicated that the physical dissolution of the crucible refractory in titanium melts was the main interaction mechanism between the crucible and the alloy melt. However, the peaks of ZrO_2 phase at 35.088°, 50.428° and 59.999° disappeared on the $BaZrO_3$ crucible surface after melting. In addition, the intensity of $BaZrO_3$ peaks at 30.238°, 43.264° and 53.687° also exhibited a decreasing trend than that of the peaks before the melting. The detailed peak values are listed in Table 3. It can be concluded that the molten alloys dissolved the second phase of ZrO_2 on the crucible surface. Furthermore, the dissolution of $BaZrO_3$ refractory caused the loose and uneven surface structure, leading to the decreased intensity of $BaZrO_3$ peaks. The XRD result shows that no interaction product was generated in the $BaZrO_3/Y_2O_3$ crucible surface after the melting. From Table 3, it can be seen that the intensity of $BaZr_{1-x}Y_xO_{3-\delta}$ peaks at 30.357°, 43.403° and 53.889° before the melting exhibited a decreasing trend than that of the peaks before the melting. However, the intensity of Y_2O_3 peaks at 29.599°, 34.269° and 49.157° exhibited an increasing trend after the melting. It appears that the molten alloy dissolved a significant amount of the $BaZrO_3$ refractory in the surface, leaving behind residual Y_2O_3 refractory, as observed in Fig. 6. Hence, the residual Y_2O_3 refractory exhibited a larger XRD intensity than $BaZrO_3$ refractory. According to the comprehensive analysis in Figs. 6 and 7, it can be concluded that the $BaZrO_3$ refractory exhibited a priority erosion phenomenon than the Y_2O_3 refractory in the surface of the $BaZrO_3/Y_2O_3$ crucible. The study by Oyama et al. [34] revealed that the thermodynamic stability of Y_2O_3 was higher than that of $BaZrO_3$. It should be noted that this interesting phenomenon might be decided by the competition erosion behavior of refractory in molten titanium alloy. It meant that the refractory with lower stability would exhibit a priority erosion phenomenon. And the relative erosion degree of the refractory in the molten titanium alloys should be declined in the following sequence: $ZrO_2 > BaZrO_3 > Y_2O_3$.

To further investigate the performance of the $BaZrO_3$ and $BaZrO_3/Y_2O_3$ crucibles for melting Ti_2Ni alloys, the microstructure images of the cross-section of the crucibles before and after melting are shown in Fig. 9. From Fig. 9a, the $BaZrO_3$ crucible before melting is observed to have a complete structure with a light-yellow color. After melting, a contact layer with a gray color, with 3190 μm in thickness, was observed in the $BaZrO_3$ crucible, as shown in Fig. 9b. The magnified SEM image of area II in Fig. 9b is shown in Fig. 9c. It can be seen that the crucible had a 485 μm thick erosion layer, confirmed by the loose and lamellar structure. During the melting, the alloy melt would erode the surface of the crucible and further permeate along the porosity in the crucible, resulting in the formation of the erosion layer. In addition, due to the capillary force, the alloy melt would further permeate into the crucible, resulting in a thicker contact layer. Figure 9d shows that the cross-section of the $BaZrO_3/Y_2O_3$ crucible before the melting also presented a complete structure. After the melting, it can be seen from Fig. 9e that a contact layer with a thickness of 3750 μm appeared in the crucible. The enlarged view of area III in Fig. 9f shows that the thickness of the erosion layer in the crucible was only 63 μm with no

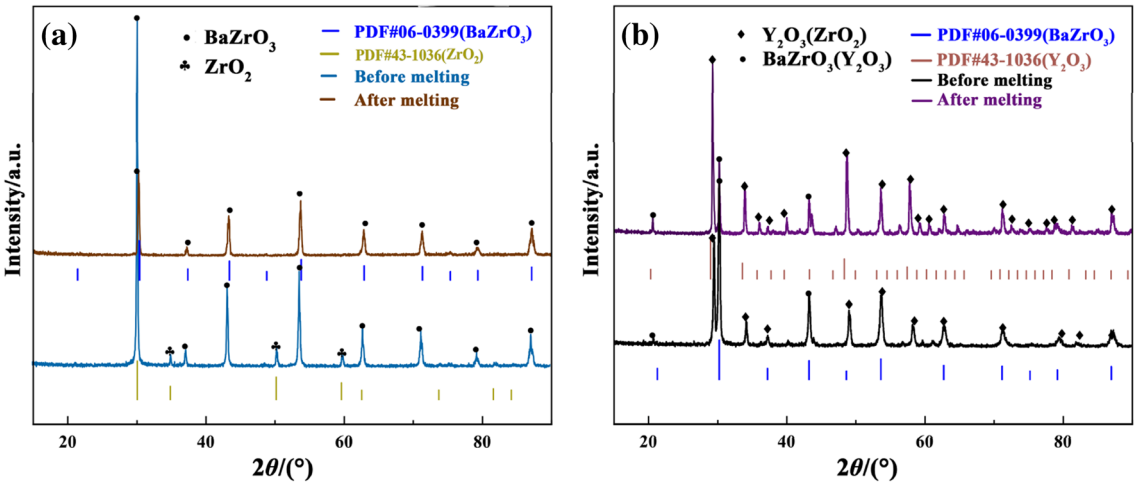

Fig. 8 XRD patterns of surface of crucibles before and after melting Ti_2Ni alloys

Table 3 Intensity of characteristic peaks of different phases in surface of crucibles

Crucible	Phase	Before melting		After melting	
		Characteristic peak (2θ/(°))	Intensity/a.u	Characteristic peak (2θ/(°))	Intensity/a.u
$BaZrO_3$	$BaZrO_3$	30.238	1799	30.24	410
		43.264	414	43.284	198
		53.687	487	53.708	273
	ZrO_2	35.088	55	–	–
		50.428	91	–	–
		59.999	54	–	–
$BaZrO_3/Y_2O_3$	$BaZrO_3$	30.357	816	29.995	372
		43.403	252	42.999	185
		53.889	239	53.401	231
	Y_2O_3	29.599	537	29.053	848
		34.269	119	33.701	246
		49.157	161	48.546	396

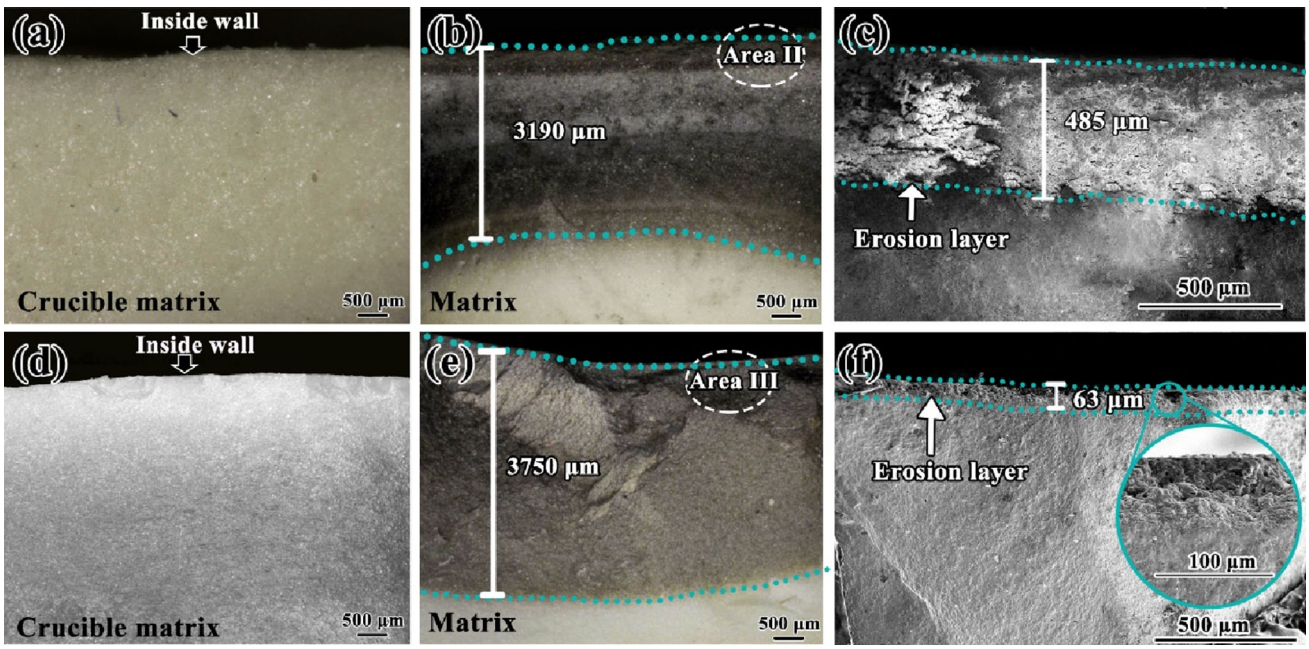

Fig. 9 Images of cross-section of crucibles. **a** $BaZrO_3$ crucible before melting; **b** $BaZrO_3$ crucible after melting; **c** magnified picture of area II in **b**; **d** $BaZrO_3/Y_2O_3$ crucible before melting; **e** $BaZrO_3/Y_2O_3$ crucible after melting; **f** magnified picture of area III in **e**

appearance of cracks. Hence, it indicates that the $BaZrO_3/Y_2O_3$ crucible exhibited a better erosion resistance to Ti_2Ni alloy melts than the $BaZrO_3$ crucible.

Figure 10 depicts the SEM images of the cross-section of the erosion layer in the $BaZrO_3$ and $BaZrO_3/Y_2O_3$ crucibles. In Fig. 10a, it can be observed that the structure of the erosion layer in the $BaZrO_3$ crucible was damaged by the alloy melts, resulting in dispersed grains. In addition, from Fig. 10a, there was no obvious ZrO_2 phase in the erosion layer, indicating that the molten alloys dissolved a large amount of phase ZrO_2, and it was in agreement with the analysis in Fig. 8. Figure 10b shows the microstructure of the erosion layer in the $BaZrO_3/Y_2O_3$ crucible. Although the Y and Zr-rich layer in the crucible was damaged by the alloy melts, this erosion layer still exhibited a relatively dense structure in comparison with that in the $BaZrO_3$ crucible. Furthermore, the $BaZrO_3/Y_2O_3$ crucible showed excellent erosion resistance to the alloy melts due to the uniform distribution of the Y, Zr, and Ba elements in the erosion layer.

Figure 11 displays the measured concentration of O, Zr and Y elements in the alloys obtained from the $BaZrO_3$ and

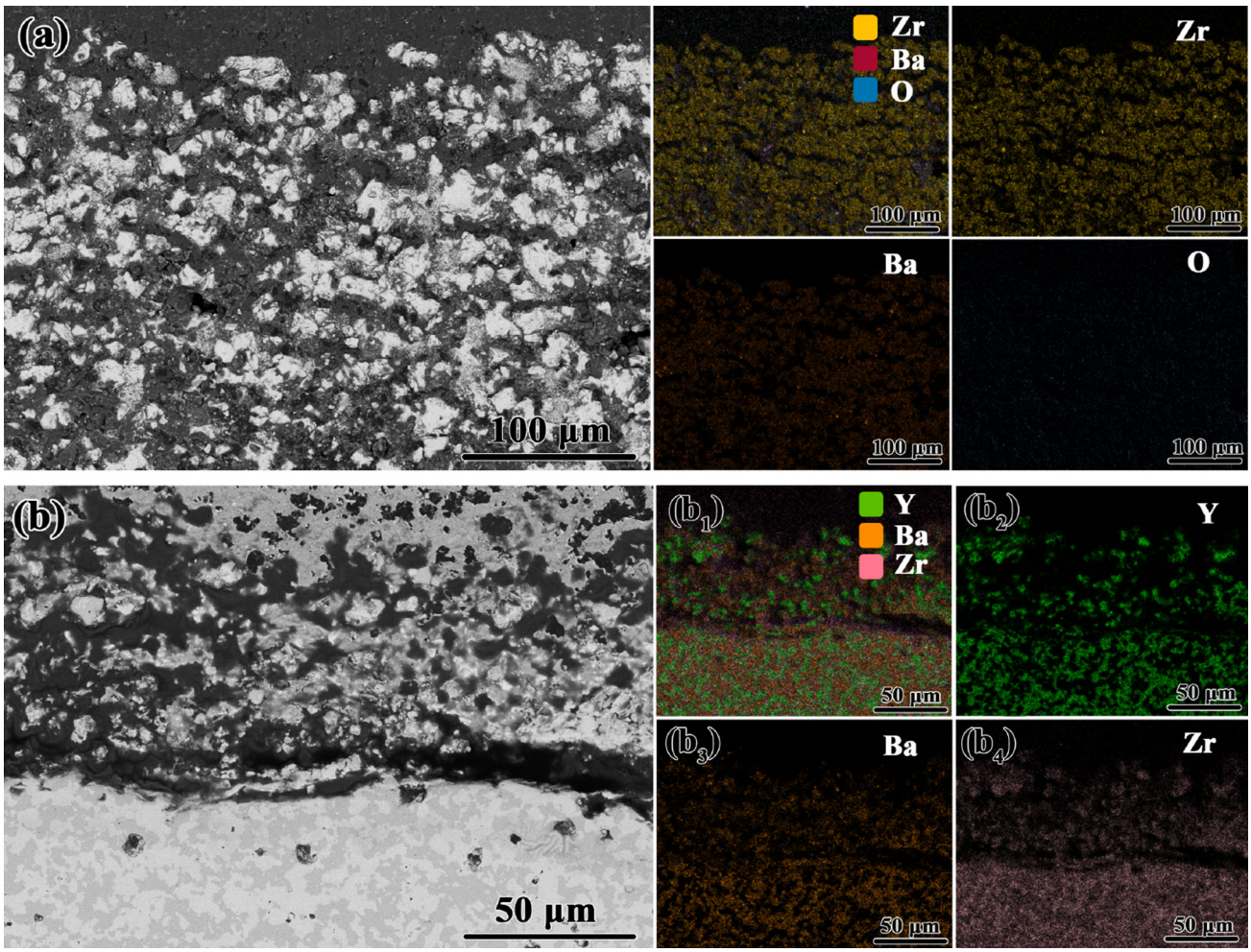

Fig. 10 SEM images and element mapping of cross-section of $BaZrO_3$ crucible (**a**) and $BaZrO_3/Y_2O_3$ crucible (**b**) after melting

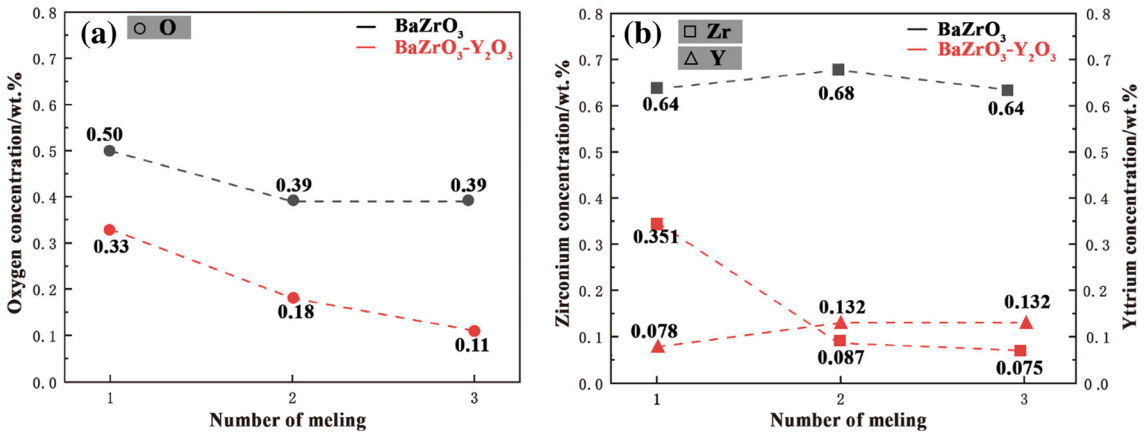

Fig. 11 Concentration of O element (**a**) and Zr and Y elements (**b**) in alloys melted in $BaZrO_3$ and $BaZrO_3/Y_2O_3$ crucibles

$BaZrO_3/Y_2O_3$ crucibles. From Fig. 11a, it can be seen that the oxygen concentration in the alloys melted in the $BaZrO_3$ crucible decreased from 0.50 to 0.39 wt.%. In addition, the alloys melted in the $BaZrO_3/Y_2O_3$ crucible also exhibited a decreased oxygen concentration (from 0.33 to 0.11 wt.%). Furthermore, as demonstrated in Fig. 11b, the Zr concentration in the alloys decreased from 0.640 to 0.635 wt.% after melting in the $BaZrO_3$ crucible. However,

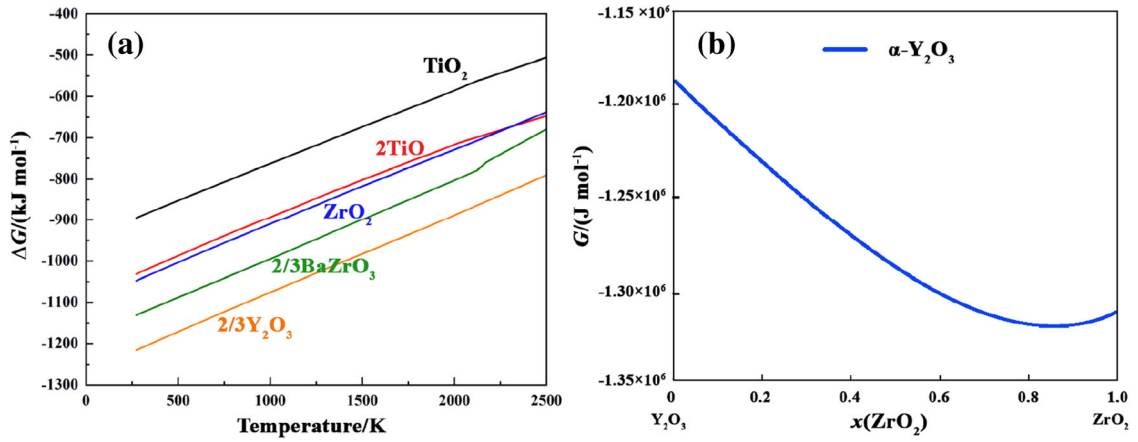

Fig. 12 Ellingham diagram of Y_2O_3, $BaZrO_3$, ZrO_2, Ti and TiO_2 (**a**) and change in Gibbs free energy (G) in solid solution region of ZrO_2–$YO_{1.5}$ binary phase diagram (**b**)

the Zr concentration in the alloys melted in the $BaZrO_3$/Y_2O_3 crucible also had a significant downward trend (from 0.350 to 0.075 wt.%). Compared to the $BaZrO_3$ crucible, the $BaZrO_3$/Y_2O_3 crucible showed less O and Zr contaminations in the alloys, indicating its superior erosion resistance to the Ti_2Ni melts. The analysis in Fig. 6 supports this conclusion by suggesting that the remaining Y_2O_3 refractory in the crucible surface had excellent erosion resistance to the Ti_2Ni melts, which prevented the further dissolution of the crucible refractory. Figure 11b shows that the Y concentration in the alloys obtained from the $BaZrO_3$/Y_2O_3 crucible was 0.078, 0.130 and 0.130 wt.%, respectively. It was because there would be some Y contamination in the alloy melts due to the presence of Y_2O_3. Apparently, the low refractory contamination of the $BaZrO_3$/Y_2O_3 crucible could reflect its good erosion resistance to the alloys.

3.3 Improved mechanism of stability of $BaZrO_3$/Y_2O_3 crucible

In our previous study [27], although the dissolution of the $BaZrO_3$/Y_2O_3 refractory was mentioned in the melting of titanium alloys, the mechanism of its improved stability was not clarified. Generally, the interaction extent between the crucible and the titanium alloy was influenced by the thermodynamic stability of the crucible refractory and the interaction kinetics [35]. Specifically, the lower Gibbs free energy of the refractory and the higher density of the crucible meant better erosion resistance.

Figure 12a shows the dependence of the change in Gibbs free energy ΔG versus the temperature for the formation of Y_2O_3, $BaZrO_3$, ZrO_2, Ti and TiO_2, which was obtained from the HSC software. Meanwhile, the Gibbs free energy of Y_2O_3 was more negative than that of $BaZrO_3$, indicating that Y_2O_3 was more stable than $BaZrO_3$. Figure 12b is about the Y_2O_3–ZrO_2 phase diagram system, which shows the change of Gibbs free energy of α-Y_2O_3 phase with the amount of ZrO_2 solid solution at 1750 °C. With the increase in ZrO_2 solid solution, the energy of the whole system decreases, and the α-Y_2O_3 phase is more stable. Thus, it can be confirmed that the stability of the $BaZrO_3$/Y_2O_3 crucible refractory was superior to that of the $BaZrO_3$ crucible refractory. Furthermore, due to the effect of the solid solution sintering, the $BaZrO_3$/Y_2O_3 crucible exhibited a high density than that of the $BaZrO_3$ crucible, confirmed by the analysis in Figs. 2 and 5. Thus, the low porosity of the $BaZrO_3$/Y_2O_3 crucible meant that it had a lower interaction rate. In summary, the $BaZrO_3$/Y_2O_3 crucible had a thinner erosion layer and a lower contamination extent to the alloy melts in comparison with the $BaZrO_3$ crucible.

Figure 13 presents a schematic of interactions between the Ti_2Ni melt and the crucible during the melting process. The dissolution of the crucible refractory damaged the structure of the crucible, leading to crucible erosion. As shown in Fig. 13a, ZrO_2 grains, which were on the surface of the $BaZrO_3$ crucible, would be totally dissolved by the alloy melts. From Fig. 13b, $BaZrO_3$ grains would be firstly dissolved, resulting in the residual Y_2O_3 grains on the surface of $BaZrO_3$/Y_2O_3 dual-phase refractory crucible. In addition, Y_2O_3 grains with higher stability could effectively resist melt erosion. Thus, the $BaZrO_3$/Y_2O_3 dual-phase refractory crucible demonstrated superior erosion resistance to Ti_2Ni alloy melts than the $BaZrO_3$ crucible.

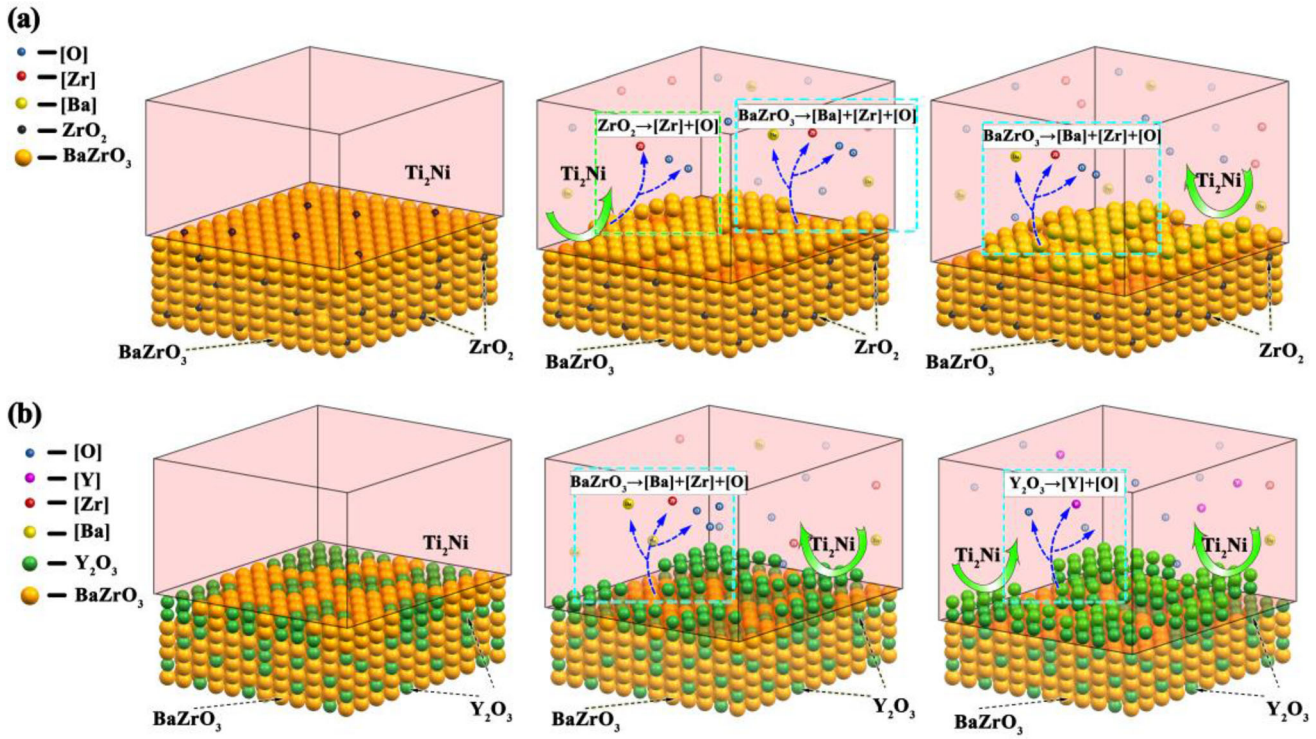

Fig. 13 Schematic diagram of interaction between crucibles and alloy melts. **a** $BaZrO_3$ crucible; **b** $BaZrO_3/Y_2O_3$ crucible

4 Conclusions

1. The $BaZrO_3/Y_2O_3$ crucible demonstrated excellent resistance to the Ti_2Ni alloy, with only a 63 μm thick erosion layer compared to the 485 μm thick layer in the fused $BaZrO_3$ crucible.
2. After melting the alloys in the $BaZrO_3$ crucible, the oxygen concentration in the alloys varied from 0.50 to 0.39 wt.%. However, the $BaZrO_3/Y_2O_3$ crucible exhibited lower refractory contamination to the alloys, and the oxygen concentration varied from 0.33 to 0.11 wt.%.
3. The improved stability of $BaZrO_3/Y_2O_3$ was attributed to the densification of the $BaZrO_3$ crucible with the Y_2O_3 addition and the generation of phase $Y_2O_3(ZrO_2)$ with higher stability. It could reduce the interaction extent of the $BaZrO_3/Y_2O_3$ crucible with Ti_2Ni alloy melts.
4. In the melting process, $BaZrO_3$ in the dual-phase refractory crucible would be firstly dissolved into the alloy melts, leading to the formation of a complete Y_2O_3 layer, which acted as a barrier to resist the erosion of the alloy melts.

Acknowledgements This work was supported by National Natural Science Foundation of China (No. 52104305) and the Science and Technology Innovation Project of Shanghai Lingang New Area (No. SH-LG-GK-2020). Additionally, we thank the anonymous referee of this paper for their constructive suggestions.

Declarations

Conflict of interest The authors declare no potential conflict of interest.

References

[1] B.P. Bewlay, S. Nag, A. Suzuki, M.J. Weimer, Mater. High Temp. 33 (2016) 549–559.
[2] M. Kaur, K. Singh, Mater. Sci. Eng. C 102 (2019) 844–862.
[3] B. Zhang, B. Ma, X. Zhang, Q. Zhu, X. Ren, Y. Zhang, X. Qu, J. Yu, J. Yu, Ceram. Int. 44 (2018) 13293–13302.
[4] V. Güther, M. Allen, J. Klose, H. Clemens, Intermetallics 103 (2018) 12–22.
[5] F. Gomes, H. Puga, J. Barbosa, C.S. Ribeiro, J. Mater. Sci. 46 (2011) 4922–4936.
[6] S. Fashu, M. Lototskyy, M.W. Davids, L. Pickering, V. Linkov, S. Tai, T. Renheng, X. Fangming, P.V. Fursikov, B.P. Tarasov, Mater. Des. 186 (2020) 108295.
[7] X. Gao, L. Zhang, X. Qu, Y. Luan, X. Chen, Vacuum 177 (2020) 109409.
[8] Q.L. Li, H.R. Zhang, Y.S. Cui, C.L. Yang, M. Gao, J.P. Li, H. Zhang, Materials 11 (2018) 1107.
[9] G.Y. Chen, B.T. Li, H. Zhang, Z.W. Qin, X.G. Lu, C.H. Li, Int. J. Appl. Ceram. Technol. 13 (2016) 1173–1181.
[10] F. Gomes, J. Barbosa, C.S. Ribeiro, Intermetallics 16 (2008) 1292–1297.
[11] R.J. Cui, M. Gao, H. Zhang, S.K. Gong, J. Mater. Process. Technol. 210 (2010) 1190–1196.

[12] M. Gao, R.J. Cui, L.M. Ma, H.R. Zhang, X.X. Tang, H. Zhang, J. Mater. Process. Technol. 211 (2011) 2004–2011.
[13] R.S. Uwanyuze, J.E. Kanyo, S.F. Myrick, S. Schafföner, J. Alloy. Compd. 865 (2021) 158558.
[14] S. Schafföner, F.G. Aneziris, H. Berek, J. Hubálková, A. Priese, J. Eur. Ceram. Soc. 33 (2013) 3411–3418.
[15] S. Schafföner, T. Qin, J. Fruhstorfer, C. Jahn, G. Schmidt, H. Jansen, C.G. Aneziris, Mater. Des. 148 (2018) 78–86.
[16] G.Y. Chen, J.Y. Kang, P.Y. Gao, Z.W. Qin, X.G. Lu, C.H. Li, Int. J. Appl. Ceram. Technol. 15 (2018) 1459–1466.
[17] L. Freitag, S. Schafföner, C. Faßauer, C.G. Aneziris, J. Eur. Ceram. Soc. 38 (2018) 4560–4567.
[18] S. Schafföner, C.G. Aneziris, H. Berek, B. Rotmann, B. Friedrich, J. Eur. Ceram. Soc. 35 (2015) 259–266.
[19] U.E. Klotz, C. Legner, F. Bulling, L. Freitag, C. Faßauer, S. Schafföner, C.G. Aneziris, Int. J. Adv. Manuf. Technol. 103 (2019) 343–353.
[20] P.Y. Gao, Y.Z. Liu, Y. Ren, G.Y. Chen, B.B. Lan, X.G. Lu, C.H. Li, Vacuum 168 (2019) 108843.
[21] J. He, C. Wei, M.Y. Li, H.B. Wang, X.G. Lu, C.H. Li, Trans. Nonferrous Met. Soc. China 25 (2015) 1505–1511.
[22] G.Y. Chen, B.B. Lan, F.H. Xiong, P.Y. Gao, H. Zhang, X.G. Lu, C.H. Li, Vacuum 159 (2019) 293–298.
[23] G.Y. Chen, Z.W. Cheng, S.S. Wang, Z.W. Qin, X.G. Lu, C.H. Li, J. Chin. Ceram. Soc. 44 (2016) 890–895.
[24] K. Liu, B.Y. Ma, P. Zhou, W.Y. Zan, C. Yu, C.J. Deng, Z.F. Wang, J. Chin. Ceram. Soc. 51 (2023) 628–634.
[25] F. Qian, H.L. Li, W.G. Yang, H.R. Guo, G.Q. Liu, H.X. Li, B.Y. Ma, J. Iron Steel Res. Int. 29 (2022) 1101–1109.
[26] L. Wang, B. Ma, X. Ren, C. Yu, C. Deng, C. Liu, C. Hu, Ceram. Int. 48 (2022) 25772–25780.
[27] G.Y. Chen, F.H. Yu, X. Hou, Y.C. Yang, B.H. Duan, Q.S. Feng, X.L. Zou, E.H. Wang, X.M. Hou, X.G. Lu, C.H. Li, Ceram. Int. 48 (2022) 20158–20167.
[28] J.P. Kuang, R.A. Harding, J. Campbell, Mater. Sci. Technol. 16 (2000) 1007–1016.
[29] Y.P. Zheng, Z. Fang, Q. Sun, E.H. Wang, M.H. Shang, W.Y. Yang, X.M. Hou, J. Phys. Chem. C 126 (2022) 2207–2213.
[30] K. Ahmed, C.A. Yablinsky, A. Schulte, T. Allen, A. El-Azab, Modelling Simul. Mater. Sci. Eng. 21 (2013) 065005.
[31] F. Wakai, M. Yoshida, Y. Shinoda, T. Akatsu, Acta Mater. 53 (2005) 1361–1371.
[32] D. Han, T. Uda, J. Mater. Chem. A 6 (2018) 18571–18582.
[33] B. Bendjeriou-Sedjerari, J. Loricourt, D. Goeuriot, P. Goeuriot, J. Alloy. Compd. 509 (2011) 6175–6183.
[34] Y. Oyama, A. Kojima, X. Li, R.B. Cervera, K. Tanaka, S. Yamaguchi, Solid State Ionics 197 (2011) 1–12.
[35] S.K. Sadrnezhad, S.B. Raz, Metall. Mater. Trans. B 36 (2005) 395–403.